

Semiclassical Structure of the Advection–Diffusion Spectrum in Mixed Phase Spaces

Christopher Amey,¹ Bala Sundaram,² and Andrew C. Poje³

¹⁾*Department of Physics, Brandeis University, Waltham, Massachusetts 02453*

²⁾*Department of Physics, University of Massachusetts, 100 Morrissey Boulevard, Boston, Massachusetts 02125*

³⁾*Graduate Faculty in Physics & Department of Mathematics, City University of New York - CSI, Staten Island, New York 10314*

(Dated: 5 February 2026)

We examine the spectral structure of the two-dimensional advection–diffusion operator in flows with mixed phase space at very large Péclet number. Using Fourier discretization combined with symmetry reduction and Krylov–Arnoldi methods, we compute on the order of one hundred leading eigenpairs reliably in the asymptotic, weak-diffusion regime. While the principal eigenvalue is asymptotically diffusive and localized on the largest regular region, the broader spectrum exhibits a rich organization controlled by local Lagrangian phase-space geometry. In particular, exponential mixing in chaotic regions rapidly suppresses correlations, whereas algebraic mixing in integrable regions generates long-lived coherent structures that dominate the slow and intermediate parts of the spectrum. We identify three distinct classes of eigenmodes: advective modes associated with transport on invariant tori, diffusive modes and, within the diffusive branch, tunneling modes arising from weak coupling between dynamically separated regular regions. Drawing on a semiclassical analogy, we assign quantum-number-like labels to these families and predict the appearance, scaling, and ordering of their sub-spectra directly from the Hamiltonian phase-space structure. The coexistence of these families implies that no uniform control of the spectral gap exists across the full spectrum: although the slowest mode is diffusive, arbitrarily small gaps arise between competing families at higher mode numbers. As a result, finite-time advection–diffusion dynamics is generically governed by persistent modal competition rather than single-mode dominance, even at asymptotically large Péclet number.

I. INTRODUCTION

The efficient mixing of passive scalars plays a fundamental role in settings ranging from industrial processing and microfluidic design to environmental and geophysical transport. In the absence of turbulence, such mixing is often achieved via *chaotic advection*, where exponential stretching and repeated folding of material lines create fine-scale gradients on which molecular diffusion can act^{1,2}. These mechanisms underlie a broad class of transport processes extending over many orders of magnitude in physical scale, from micrometer-scale microfluidic mixers^{3,4} to planetary atmospheres and oceanic flows where coherent vortices and jets inhibit tracer dispersion and lead to anomalous transport^{5,6}.

Realistic time-dependent flows exhibit a wide range of dynamical behavior depending on their kinematic structure. At one extreme lie globally integrable flows, where trajectories are confined to invariant tori and material elements experience only algebraic deformation in time. In this setting the advection–diffusion operator decomposes naturally into an axisymmetric sector, which is self-adjoint and purely diffusive with decay rates $\gamma \sim Dk^2$ (or equivalently, $\gamma \sim Pe^{-1}$), and non-axisymmetric sectors that remain intrinsically non-self-adjoint. Rigorous semiclassical analysis shows that these advective sectors support families of modes whose decay rates scale anomalously as $Pe^{-1/2}$ or $Pe^{-1/3}$, depending on the local structure of the frequency map.

At the opposite extreme lie globally chaotic flows. For uniformly hyperbolic systems, rigorous analysis establishes logarithmic enhanced dissipation with decay rates $\gamma \sim \log(Pe)^7$. More generally, in non-uniformly hyperbolic chaotic systems, strong spatial and tem-

poral variability in stretching rates produces rich spectral structure including strange eigenmodes⁸ and multifractal scalar measures^{9–11}. In such flows, the spectrum of the one-period advection–diffusion operator reflects the distribution of finite-time Lyapunov exponents and the history of filamentation^{12–14}.

Between these extremes lie *mixed phase spaces*, in which chaotic regions coexist with dynamically invariant regular islands surrounding elliptic fixed points or invariant tori. These islands support algebraic deformation and long-lived coherent structures, introducing a second, qualitatively distinct transport mechanism within the same operator. Mixed phase spaces therefore combine three competing mechanisms within a single dynamical system: non-uniformly hyperbolic chaos, algebraic transport on regular sets, and diffusion across their boundaries. How these mechanisms jointly shape the spectrum of the advection–diffusion operator—beyond the leading eigenvalue—remains a central unresolved problem.

Significant progress has been made toward understanding aspects of this competition. Coarse-grained transfer-operator and mapping-matrix approaches have demonstrated that, at very large effective Péclet numbers, dominant decay modes localize on regular islands in flows with strongly chaotic components^{4,15–18}. Gorodetskyi et al. demonstrated that this localization persists even when regular regions occupy arbitrarily small fractions of phase space, provided the diffusive length scale remains smaller than the characteristic island width. These computational methods establish that the asymptotic decay in mixed phase spaces is controlled by island-localized, diffusive modes.

Popovych et al.¹¹ observed that in certain parameter regimes where multiple eigenvalues are nearly degenerate, the resulting modal competition produces non-exponential decay over finite times, with eigenmodes localizing on elliptic islands or boundaries between weakly connected chaotic regions. However, they found the occurrence of such near-degeneracies to vary unpredictably in the 2D parameter space of their model.

Complementing these computational results, rigorous semiclassical analysis of integrable advection–diffusion operators has established the theoretical foundation for anomalous scaling in regular flows^{19–21}. These results provide sharp mathematical proofs that advective sectors in integrable flows support families of modes with $\text{Pe}^{-1/2}$ or $\text{Pe}^{-1/3}$ decay rates—the so-called advection-enhanced diffusion regime—with the specific exponent determined by local geometric structure near elliptic fixed points. However, these analyses rely on global action-angle coordinates and do not extend to mixed phase spaces where multiple island chains coexist with chaotic regions.

Extending these insights to systems with multiple coexisting regular regions of different scales presents both computational and conceptual challenges. Computational methods have established asymptotic localization and observed near-degeneracies in specific cases, while rigorous analysis provides scaling laws for globally integrable flows. What remains unexplained is how the full spectrum organizes when several island chains compete: which modes dominate finite-time dynamics, when spectral gaps collapse, and in particular, when and why competing island families produce near-degenerate eigenvalues. Addressing these questions requires an interpretive framework capable of predicting spectral organization from the underlying phase-space geometry.

The advection–diffusion operator admits a semiclassical interpretation. In this analogy, the diffusivity D plays the role of an effective Planck constant, so that the limit $\text{Pe} \rightarrow \infty$ corresponds to $\hbar_{\text{eff}} \rightarrow 0$. Regular islands act as finite potential wells supporting diffusive modes with Pe^{-1} scaling, while elliptic cores behave as harmonic oscillators producing advective mode families with $\text{Pe}^{-1/2}$ spacing. The chaotic sea mediates weak coupling between these families, giving rise to tunneling-like hybridization when wells approach degeneracy. This interpretation identifies geometric quantities—*island size* and *core curvature*—as the fundamental parameters controlling spectral organization, and provides a predictive framework for when distinct spectral branches arise and how they scale.

In this work, we compute the leading eigenvalues and eigenmodes of the one-period advection–diffusion operator for the Chirikov standard map at Péclet numbers up to 10^7 . We show that the spectrum organizes into universal families—diffusive modes localized on islands, advective modes concentrated at elliptic cores, and hybrid modes spanning multiple

regions—whose multiplicity and ordering can be predicted directly from phase-space geometry. When diffusive ladders associated with distinct islands approach one another, avoided crossings produce mixed states exhibiting the characteristic splittings of semiclassical tunneling. Importantly, although the slowest mode is ultimately diffusive and island-localized, the coexistence and hybridization of these families precludes uniform control of spectral gaps: arbitrarily small gaps arise between competing families at higher mode numbers, and finite-time dynamics is generically governed by persistent modal competition rather than single-mode dominance.

These results demonstrate that the local Hamiltonian geometry of the Lagrangian phase space determines the organization of the advection–diffusion spectrum. The semiclassical framework developed here provides both a classification scheme for eigenmodes in mixed systems and quantitative predictions for their appearance, validated by direct computation at asymptotically large Péclet numbers.

II. MODEL AND SPECTRAL FORMULATION

We consider the initial-value problem for the advection–diffusion equation on the two-torus $\mathbb{T}^2 = [0, 2\pi]^2$,

$$\frac{\partial \rho}{\partial t} + \vec{u}(x, t) \cdot \nabla \rho = D \nabla^2 \rho, \quad x \in \mathbb{T}^2, \quad t > 0, \quad (1)$$

with prescribed initial condition

$$\rho(x, 0) = \rho_0(x), \quad x \in \mathbb{T}^2, \quad (2)$$

and periodic boundary conditions in both spatial directions. Here $\rho(x, t)$ is a passive scalar, $D > 0$ is the molecular diffusivity, and $\vec{u}(x, t)$ is a given, divergence-free, time-periodic velocity field with period T .

Throughout, \vec{u} is generated by the Chirikov–Taylor standard map²². This provides a canonical setting in which integrable, mixed, and strongly chaotic phase-space structures can coexist within a single model, allowing us to probe how the spectral properties of the advection–diffusion operator reflect the underlying Hamiltonian geometry of the flow. The map arises from the time-periodic stream function

$$\psi(x, y, t) = \frac{y^2}{2} + K \cos x \sum_{n=-\infty}^{\infty} \delta(t - nT), \quad (3)$$

where $\delta(t)$ is the Dirac delta function and the parameter K controls the dynamics: $K = 0$ is integrable, intermediate values yield mixed phase spaces containing both chaotic seas and regular islands, and $K \rightarrow \infty$ approaches the anti-integrable limit with globally chaotic dynamics.

Temporal periodicity allows the dynamics to be expressed in terms of the one-period evolution operator U ,

$$\rho(r, t + T) = U(T)\rho(r, t). \quad (4)$$

Writing $\rho(r, t) = e^{\mu t}\phi(r, t)$ with ϕ periodic in time yields the eigenvalue problem

$$U\phi = e^{\mu t}\phi \equiv \lambda\phi, \quad (5)$$

so that the spectrum of U determines decay rates and spatial structure of all modes. Because diffusion renders U non-unitary, $|\lambda| < 1$. Throughout this work we characterize eigenvalues in terms of the decay rate

$$\gamma = -\frac{1}{T} \log |\lambda|, \quad (6)$$

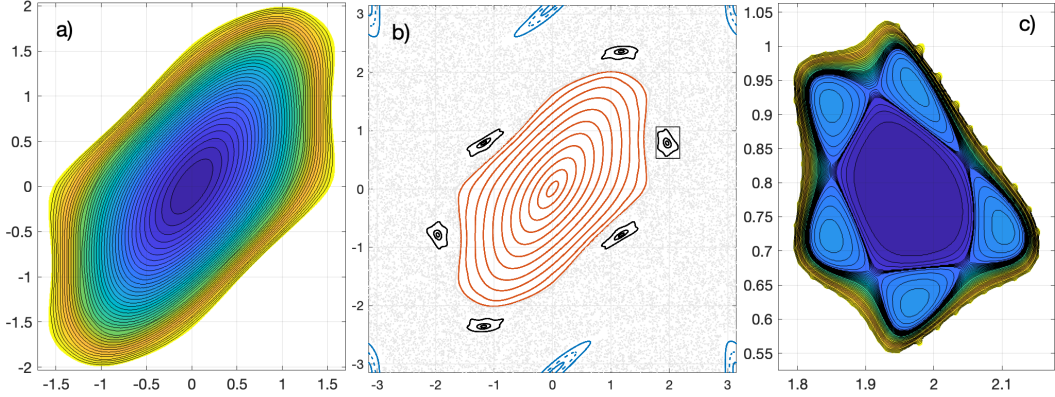


FIG. 1. Local integrable structure of the standard map at $K = 1.7$. (a) Effective Hamiltonian $H_{\text{eff}}(x, y)$ reconstructed on the period-1 island, shown as filled contours. (b) Poincaré section of the map, with chaotic trajectories in gray and selected invariant curves outlining the period-1 (red), period-2 (blue) and period-6 (black) island chains. (c) Effective Hamiltonian $H_{\text{eff}}(x, y)$ reconstructed on a single lobe of the period-6 chain shown zoomed on the black box in panel (b). In panels (a) and (c), H_{eff} is normalized to $[0, 1]$ and displayed only on the corresponding regular region.

which reduces to $\gamma = -\log |\lambda|$ for the unit period $T = 1$ used in all computations. The dominant eigenvalue governs the asymptotic decay, but at finite times the scalar field typically reflects contributions from multiple eigenmodes; this becomes increasingly important as Pe grows and spectral gaps shrink.

The stroboscopic dynamics admits a split-operator representation. Starting from Liouville's equation

$$\frac{\partial \rho}{\partial t} + i\hat{L}(t)\rho = 0, \quad (7)$$

with Liouvillian

$$i\hat{L}(t) = \frac{\partial \psi}{\partial y} \frac{\partial}{\partial x} - \frac{\partial \psi}{\partial x} \frac{\partial}{\partial y} = \vec{u} \cdot \nabla, \quad (8)$$

the delta-function forcing yields the one-period advective operator

$$\rho^{(t+T)}(x, y) = \exp\left(-y \frac{\partial}{\partial x} - K \sin x \frac{\partial}{\partial y}\right) \rho^{(t)}(x, y). \quad (9)$$

Including diffusion and working in Fourier space gives the full one-cycle advection-diffusion operator in the form

$$\rho^{(t+T)}(m, n) = \sum_{k=-\infty}^{\infty} J_{m-k}(nK) \rho^{(t)}(k, k+n) e^{-D(m^2+n^2)}, \quad (10)$$

where J_ℓ denotes a Bessel function of the first kind. The diffusive factor exponentially suppresses large wavenumbers, permitting truncation to a finite Fourier basis. As D decreases, the required truncation grows rapidly, making the large- Pe regime computationally demanding.

Our objective is to compute and interpret a substantial portion of the spectrum of the advection-diffusion operator at large Péclet numbers. We compute leading eigenpairs using an implicitly restarted Arnoldi method, and show that the resulting eigenmodes organize into distinct diffusive, advective, and mixed families whose scaling, multiplicity, and ordering are dictated by the underlying Lagrangian phase-space geometry. Details of the numerical implementation, including convergence diagnostics and resolution considerations, are given in Appendix A.

III. PHASE-SPACE STRUCTURE AT $K = 1.7$

We focus on the standard map at $K = 1.7$, a prototypical mixed phase space. At this parameter value, three prominent island chains of period 1, 2, and 6 coexist with a substantial chaotic sea. Figure 1 shows this structure and introduces the geometric objects that organize the spectrum.

Panel (b) shows a Poincaré section of the map, with chaotic trajectories in gray and selected invariant curves outlining the dominant regular regions. The period-1 island occupies the central region, while smaller chains of period 2 and period 6 are embedded in the surrounding chaotic sea. These regular regions form the non-chaotic components of the Lagrangian dynamics.

Panels (a) and (c) display effective Hamiltonians $H_{\text{eff}}(x, y)$ reconstructed on representative regular regions: the period-1 island and a single lobe of the period-6 chain, respectively. In each case, H_{eff} provides a local integrable surrogate for the map, with level sets approximating invariant curves in the corresponding region. The period-1 island appears as a smooth, nearly quadratic well, whereas the period-6 lobe exhibits pronounced non-quadratic structure associated with internal resonances. Details of the numerical reconstruction of the local Hamiltonian structure are given in Appendix B.

IV. FINITE-TIME DYNAMICS AT LARGE PÉCLET NUMBER

To motivate the need for a spectral description beyond the dominant eigenmode, we examine the finite-time evolution of simple, localized disturbances under the advection-diffusion operator at $D = 10^{-6}$. We focus on global homogenization: how a localized patch of scalar, initially in the chaotic sea, is transported and injected into regular components of phase space.

We consider two initial conditions constructed from the same compactly supported Gaussian $G(x, y)$ centered at (x_0, y_0) ,

$$\rho_1(x, y, 0) = \partial_x G(x, y), \quad \rho_2(x, y, 0) = \partial_y G(x, y).$$

Both fields are localized on the same spatial scale, have zero spatial mean, and are supported in the same region of the chaotic sea. They differ only by a $\pi/2$ rotation in the orientation of their gradients. Any difference in their long-time behavior must therefore arise not from where the scalar is placed, but from how the early-time advective dynamics transports it into regular sets.

Figure 2 shows the evolution of these two initial conditions over 1200 periods. In both cases, the scalar is rapidly homogenized within the chaotic sea and progressively accumulates inside the primary elliptic island. At late times the fields occupy the same geometric support: the same island core, the same surrounding invariant manifolds, and the same hierarchy of filaments. What differs is not which structures are present, but the relative amplitudes with which they are populated. These weights are set during the early advective stage, when material originating in the chaotic region is injected into regular regions in a manner that depends sensitively on the orientation of the initial gradients.

This distinction is dynamically relevant. Figure 3 shows that the L^2 norms of the two solutions decay at persistently different rates over the entire accessible time window. Even after 10^3 periods—orders of magnitude longer than any advective time scale—the system has not collapsed onto a unique decay rate. Although both solutions occupy the same geometric subspace, they project onto different combinations of long-lived modes.

The implication is fundamental: at large Péclet number and finite times, the dynamics is not governed by a single dominant eigenmode. What remains relevant is a collection of slowly decaying modes associated with the same regular structures, whose relative weights are determined by how the initial density is transported from the chaotic sea into those regions. Understanding the dynamics therefore requires access to a leading portion of the spectrum and to the organization of these long-lived families.

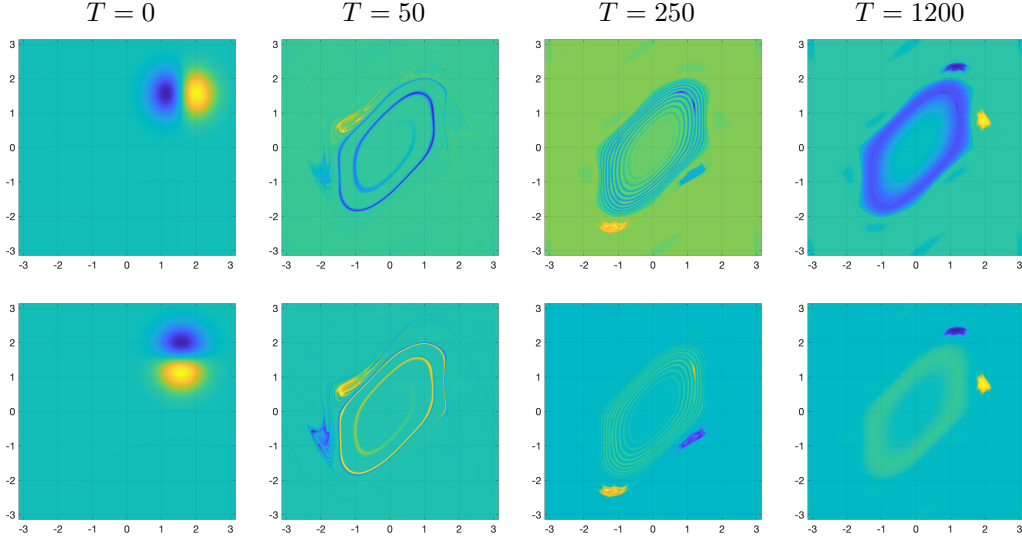


FIG. 2. Evolution of two localized initial conditions under the advection-diffusion operator for $K = 1.7$, $D = 10^{-6}$. The two rows correspond to $\rho_1 = \partial_x G$ (top) and $\rho_2 = \partial_y G$ (bottom), where G is the same Gaussian centered at (x_0, y_0) . Columns show the initial condition and the fields after $n = 50$, 250 , and 1200 periods.

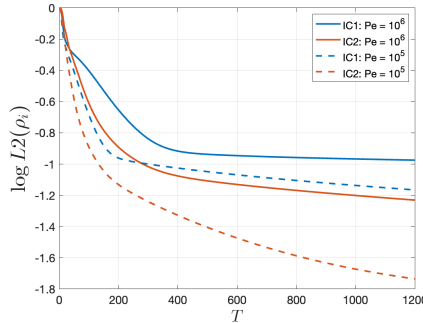


FIG. 3. Time evolution of the L^2 norm of the scalar fields shown in Fig. 2. Solid curves correspond to $\text{Pe} = 10^6$, dashed curves to $\text{Pe} = 10^5$. Blue curves show $\rho_1 = \partial_x G$; red curves show $\rho_2 = \partial_y G$.

V. GLOBAL STRUCTURE OF THE COMPUTED SPECTRUM

For each Péclet number we compute a fixed number of leading eigenpairs $U\phi = \lambda\phi$, where U advances the scalar field by one forcing period. Because U is non-unitary for $D > 0$, all eigenvalues satisfy $|\lambda| < 1$. We represent the spectrum in polar coordinates

$$\theta = \arg(\lambda), \quad \gamma = -\log|\lambda|, \quad (11)$$

where γ is the exponential decay rate and the unit circle maps to $\gamma = 0$. This transformation unwraps the complex plane into a strip in which eigenvalues at different Péclet numbers can be compared on a common scale.

Figure 4 shows the leading spectra for $\text{Pe} = 10^5$, 10^6 , and 10^7 in these coordinates. Three features emerge immediately. First, the spectrum is far from a featureless cloud. Eigenvalues organize strongly in phase, with pronounced vertical alignments that persist across all three Péclet numbers. The solid vertical guide lines mark $\theta = 0, \pi/3, 2\pi/3$, and π , corresponding to the dominant period-1, 2, and 6 island chains visible in the phase portrait.

These angles are not arbitrary plotting artifacts but are tied to geometric structures in the underlying map.

Second, the real axis $\theta = 0$ plays a special role. Eigenvalues associated with all three island periods appear there, so this column does not correspond to a single dynamical mechanism or period. Distinct geometric origins are already interleaved in decay rate at the most prominent phase.

Third, increasing Péclet number does not simply sharpen a fixed set of branches. As D decreases, additional eigenvalues appear increasingly close to the unit circle, populating phase angles that were previously sparse or empty. Because we compute a fixed number of leading eigenpairs at each Pe , these plots represent a moving window into an ever denser near-unit-circle spectrum: higher Péclet numbers reveal more angular variety, while the apparent prominence of any individual alignment reflects sampling rather than intrinsic importance.

As $D \rightarrow 0$, the advection operator admits continuous spectral components on the unit circle, and the discrete spectrum of the diffusive problem progressively resolves this dense set of phases. At finite D , however, the spectrum remains discrete, and the question is how these accumulating eigenvalues organize in relation to the underlying phase-space geometry.

VI. SPECTRAL FAMILIES AND UNIVERSALITY IN MIXED PHASE SPACE

The spectra in Fig. 4 reveal distinct, persistent branches. What appears at first glance as a dense cloud of eigenvalues separates into organized families. Modes clustered along the symmetry directions $\theta = m\pi/3$ form discrete ladders, color-coded in Fig. 4 by island family and identified in the caption as diffusive modes $\psi_{m,k}^p$. Between these axes lie advective modes ϕ , occupying distinct phases from those of the diffusive branches.

Eigenvalues that align along a given branch correspond to eigenfunctions with closely related spatial structure and common dynamical origin, while modes in different regions of the spectrum exhibit qualitatively different morphology. The spectrum therefore decomposes naturally into a small number of spectral families, each tied to a distinct transport mechanism in the mixed phase space. We make this classification explicit and show that the internal organization of each family is universal across Pe .

A. Diffusive Modes

We begin with the modes clustered along the symmetry axes in Fig. 4, which are governed primarily by diffusion within regular islands.

1. Island-localized modes

Figures 5 and 6 show representative eigenfunctions supported on individual regular islands. These modes occupy the full extent of a single island and closely resemble eigenfunctions of the Laplacian on a bounded domain. Their nodal patterns form approximately concentric bands across the island interior, with successive modes distinguished primarily by the number of such bands. In this sense, each regular island acts as a finite square well for the diffusive dynamics.

Dirichlet boundary conditions emerge naturally from the dynamics. Trajectories in the chaotic sea decorrelate rapidly and homogenize ρ on timescales short compared with diffusion across an island. From the perspective of the island interior, the exterior therefore acts as a nearly uniform reservoir. Diffusive structure within the island is continually leaked into this well-mixed background, so that the island boundary behaves, to leading order, like a fixed-value interface. Each regular island thus forms a deep diffusive well embed-

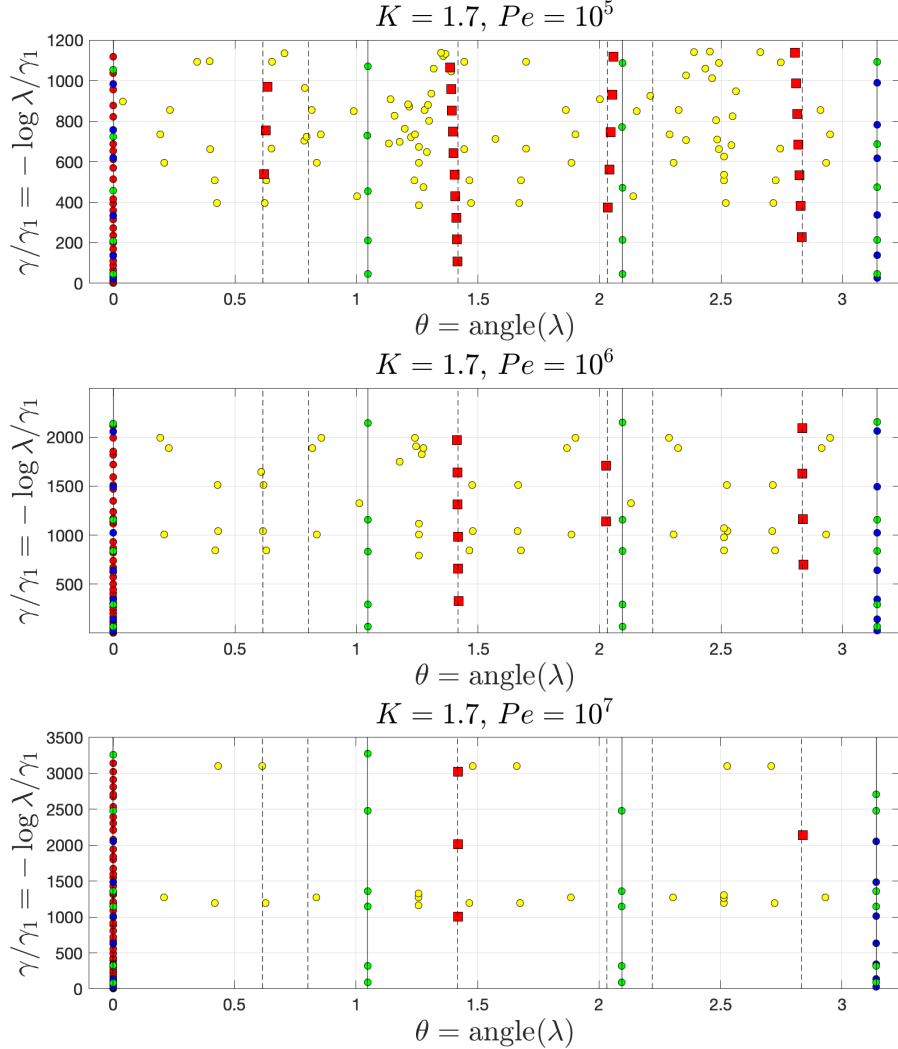


FIG. 4. Leading eigenvalues of the one-period advection-diffusion operator for $Pe = 10^5$, 10^6 , and 10^7 , plotted in polar form using $\theta = \arg(\lambda) \in [0, \pi]$ (folded by complex-conjugate symmetry) and $\gamma = -\log |\lambda|$, normalized in each panel by the leading decay rate γ_1 . Solid vertical lines mark the symmetry directions $\theta = m\pi/3$ ($m = 0, 1, 2, 3$), corresponding to the roots of unity associated with the dominant period-1, 2, and 6 island chains. Colored circles denote diffusive eigenmodes $\psi_{m,k}^p$, grouped by island family p ($p = 1, 2, 6$) and clustered along these symmetry directions, forming discrete diffusive ladders. Red squares identify advective modes ϕ , which lie away from the symmetry axes and populate the spectral gaps between diffusive branches. Dashed vertical lines indicate the independently computed advection phases obtained from the mean rotation number $\rho(I)$ of invariant tori within the period-1 island.

ded in a homogenizing environment, and its island-filling modes are naturally organized as eigenfunctions of a Dirichlet Laplacian on a bounded domain.

A period-1 island, a period-2 island, and a period-6 island all support this same square-well family, even though the spatial extent and layout of the islands differ. Within any given island, the dominant organizing parameter is therefore a radial mode index.

For islands of period $p > 1$, this family further splits into p symmetry classes, reflecting how the mode is phased across the p dynamically equivalent copies of the island. A period-2 island, for example, admits two such classes, corresponding to global phases 0 and π under interchange of the two lobes. More generally, $m \in \{0, \dots, p-1\}$ labels these discrete phase

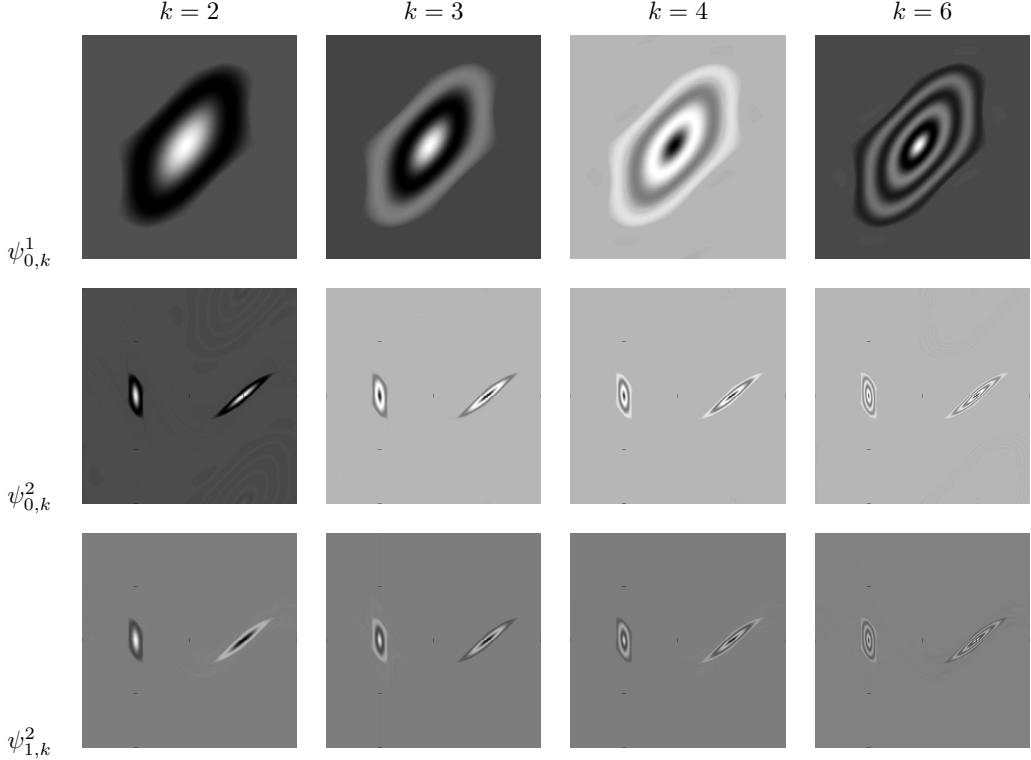


FIG. 5. Three families of diffusive modes for $K = 1.7$, $D = 10^{-6}$. Top row: Period-1 modes $\psi_{0,k}^1$ at $k = 2, 3, 4, 6$. Bottom two rows: Period-2 modes $\psi_{m,k}^2$ at the same k -values in both symmetry classes ($m = 0, 1$) (For clarity, Period-2 modes are unwrapped on the torus and plotted in $(\bar{x} = x + \pi/2, \bar{y} = y - \pi)$).

classes.

We denote this family by $\psi_{m,k}^p$ where p is the island period, k counts radial nodes, and m labels the discrete phase class associated with the p -fold geometry.

Diffusion across a bounded region imposes Dirichlet scaling,

$$\gamma_k(\psi^p) \sim D k^2. \quad (12)$$

Figure 7 shows the isolated diffusive ladders for the dominant period-1, 2, and 6 island chains at $\text{Pe} = 10^7$ where the decay rates are multiplied by the computed area of single lobe each island chain. As expected for Laplacian-like modes on bounded domains, each ladder is approximately quadratic in the radial index k , with the overall scale set by island size,

$$\gamma_k^{(p)} \sim D \frac{k^2}{A_p},$$

up to a shape factor. Smaller islands therefore exhibit faster decay at fixed k and steeper ladders, consistent with the ordering $A_1 \gg A_2 \gg A_6$. The shorter extent of the period-2 and period-6 ladders reflects weaker confinement: fewer well-localized diffusive levels remain before leakage into the chaotic sea and inter-island interactions become significant.

Equation (12) is an asymptotic statement. The single radial index k is only a coarse proxy for the two-dimensional geometry of a finite island, and the effective Laplacian felt by these modes depends on details of the island boundary that vary weakly with D . At small k in particular, curvature, anisotropy, and boundary structure introduce order-one corrections to the simple square-well picture. The ladder $\{\psi_{m,k}^p\}$ should therefore be understood as an organizing framework, not as an exact spectrum of an isolated operator.

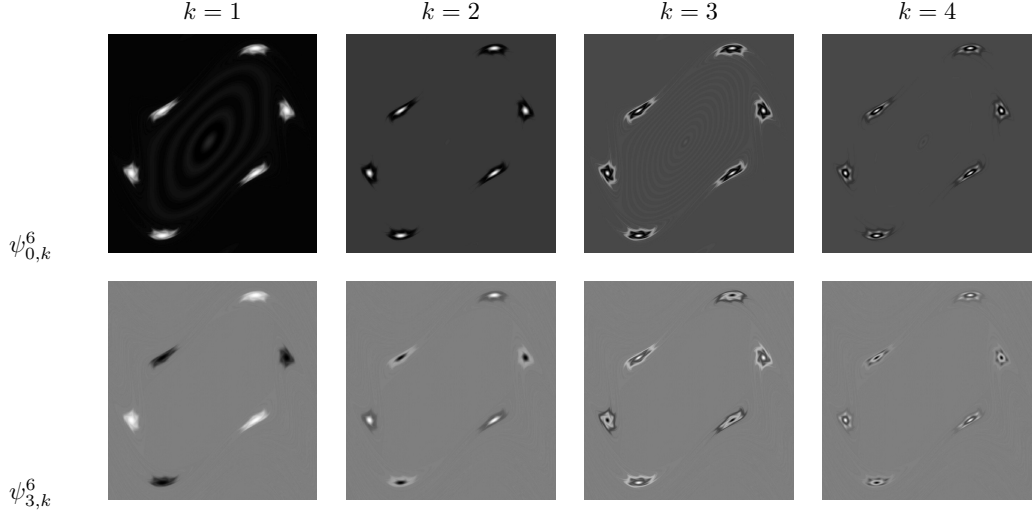


FIG. 6. Leading diffusive modes in the period 6 island chain for $K = 1.7$, $D = 10^{-6}$ for $m = 0, 3$ symmetry classes.

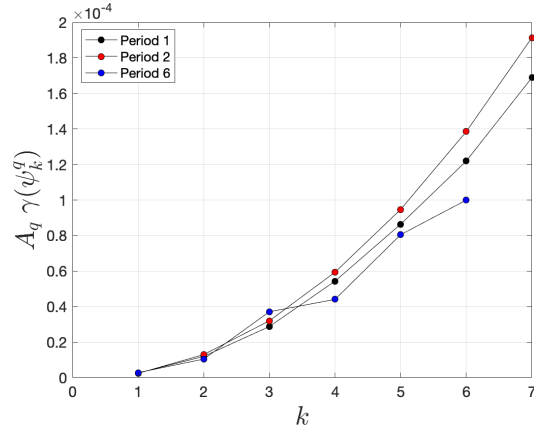


FIG. 7. Area-rescaled diffusive ladders at $\text{Pe} = 10^7$ for the period-1, 2, and 6 island chains.

More importantly, the phase space contains multiple regular island chains, each supporting its own diffusive ladder. Nothing in the construction of these families enforces a spectral separation between ladders associated with different islands. It is therefore inevitable that, for some pairs of indices,

$$\gamma(\psi_{m,k_p}^p) \approx \gamma(\psi_{m,k_q}^q),$$

even when the underlying islands are dynamically distinct. These near coincidences in decay rate set the stage for interactions between ladders that lie beyond the single-island picture.

2. Inter-island hybridization and avoided crossings

The diffusive ladders $\{\psi_{m,k}^p\}$ described above are defined by localization on a single regular island chain and by the quadratic scaling $\gamma \sim \alpha_{p,m} D k^2$. This description is asymptotically correct in the limit of weak coupling between dynamically distinct regions. At finite Pe , however, the spectrum is not a direct sum of independent island ladders. As k increases,

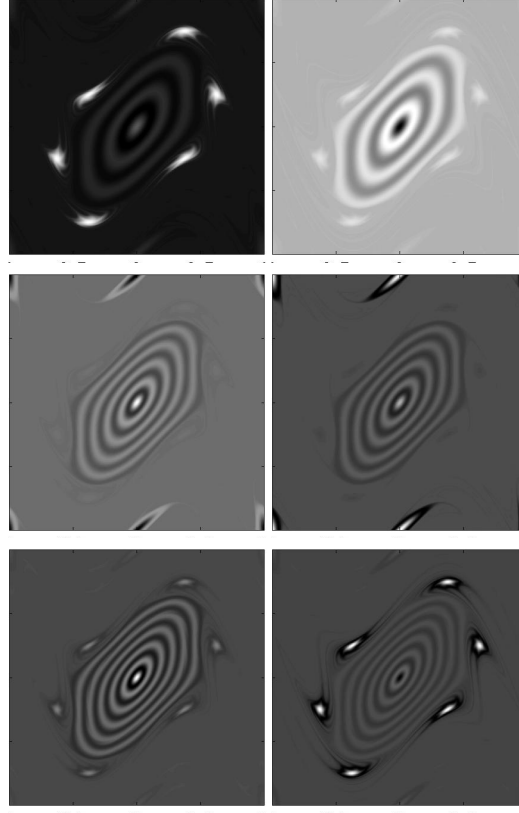


FIG. 8. Leading pairs of hybrid (tunneling) diffusive eigenmodes spanning multiple islands at $\text{Pe} = 10^5$. Each row shows the two hybrid eigenmodes associated with a single period-1 diffusive mode, $\psi_{0,k}^1$, split by coupling to a diffusive mode in the secondary island chain. Top row: $\psi_{0,6}^1/\psi_{0,1}^6$ pair. Middle: $\psi_{0,10}^1/\psi_{0,2}^2$. Bottom: $\psi_{0,12}^1/\psi_{0,2}^6$ pair.

the decay rates of different ladders inevitably approach one another, and the assumption of isolation breaks down.

When two diffusive levels,

$$\gamma(\psi_{0,k}^1) \approx \gamma(\psi_{m,k_p}^p),$$

come into near degeneracy, the corresponding eigenfunctions no longer remain confined to their parent islands. Instead, the eigenvalue problem produces a pair of modes whose support spans both regular regions. Each member of the pair carries comparable weight on the two islands, but with opposite relative phase. In direct analogy with symmetric and antisymmetric combinations in tunneling problems, the near-degeneracy is lifted into two distinct eigenmodes with closely spaced decay rates.

Figure 8 shows the leading examples of this process at $\text{Pe} = 10^5$. Each row corresponds to a single period-1 diffusive ladder level $\psi_{0,k}^1$ that has entered near resonance with a diffusive level on a secondary island chain. The two panels in a row are the split descendants of that one ladder level: hybrid eigenmodes that differ only in their relative phase across islands. What would be a single diffusive mode in the uncoupled limit thus appears in the full problem as a paired structure.

These hybrid modes mark the breakdown of the single-island ladder picture. They are neither members of the period-1 family nor of the secondary ladder alone, and they do not obey either island's diffusive scaling law. Spectrally, they occupy the narrow gaps opened by avoided crossings between ladders. Geometrically, they represent tunneling of diffusive structure across invariant barriers separating regular regions.

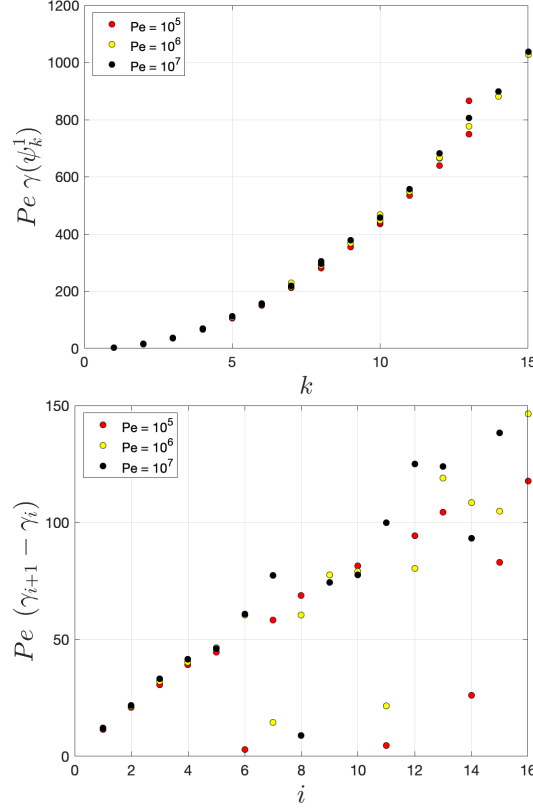


FIG. 9. (top) Scaled decay rates $Pe \gamma(\psi_k^1)$ for the period-1 diffusive family (including hybridized modes) at $Pe = 10^5, 10^6, 10^7$, plotted against the radial ladder index k . (bottom) Consecutive scaled gaps $Pe (\gamma_{i+1} - \gamma_i)$ along the same branch, where the modes are ordered by increasing γ .

As Pe increases, the diffusive resolution scale shrinks and most near-degeneracies between diffusive ladders produce only weak leakage between branches. Hybridization is confined to a sparse, geometrically selected set of ladder levels. In the small- D limit the spectrum is well approximated by a direct sum of island families. The only systematic exceptions occur at isolated (k_1, k_p) pairs where geometric commensurability is most precise. At those locations, genuinely mixed eigenmodes persist even as $D \rightarrow 0$.

3. Diffusive Scaling

Figure 9 shows two complementary aspects of the dominant diffusive branch. The upper panel shows that, once scaled by Pe , the period-1 ladder collapses onto a single curve across three decades in Pe . This collapse holds even in the presence of hybridized levels, confirming that the $\theta = 0$ branch constitutes a single, universal diffusive family, consistent with the island localization demonstrated by Gorodetskyi et al.^{17,18}. Hybridization modifies individual levels, but it does not destroy the identity of the ladder as a whole.

The lower panel reveals a more delicate consequence of inter-island coupling. Although the backbone of the ladder follows the expected diffusive trend, the spacing between successive modes is punctured by isolated, persistent collapses. These anomalously small gaps occur at fixed locations in the ordering for all Pe and correspond to hybridized levels. Thus, even on the simplest and most dominant branch of the spectrum, the presence of multiple island chains removes any control over spectral gaps. The law $\gamma \sim Dk^2$ governs the coarse organization of the ladder, but it does not determine its fine structure.

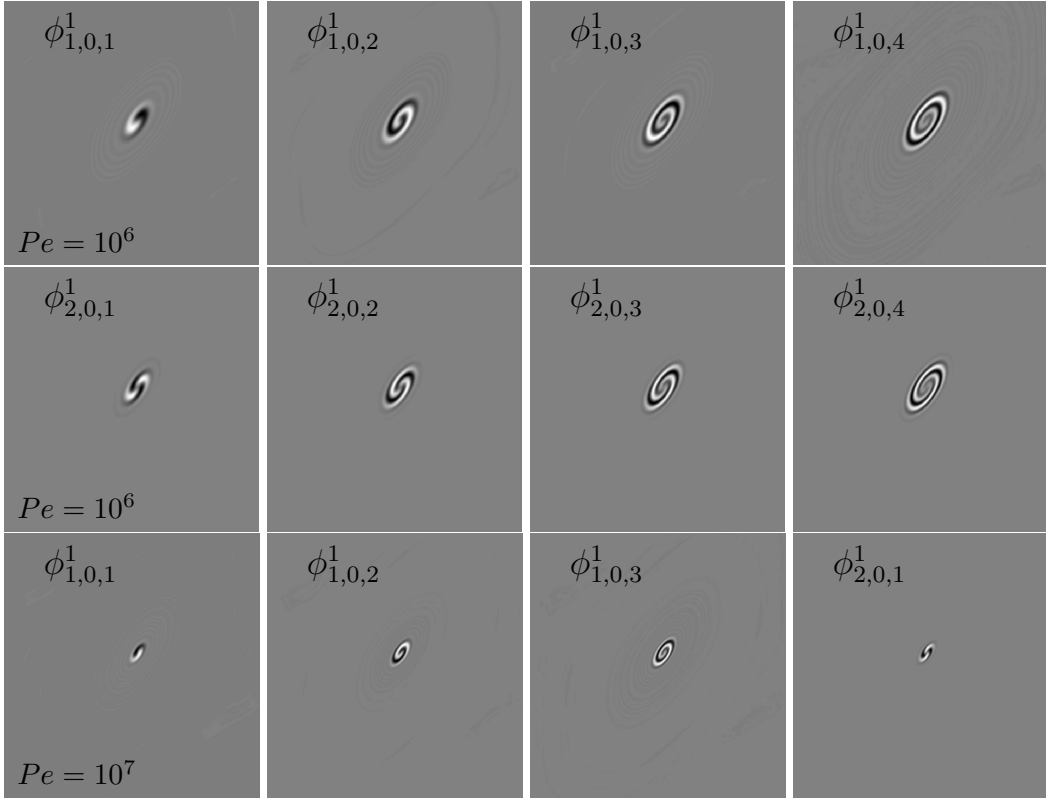


FIG. 10. Advective (core-localized) modes in the period-1 island for $K = 1.7$. Top two rows: $D = 10^{-6}$, azimuthal families $\phi_{1,0,k}^1$ ($q = 1$) and $\phi_{2,0,k}^1$ ($q = 2$) for $k = 1, 2, 3, 4$. Bottom row: $D = 10^{-7}$, showing $\phi_{1,0,k}^1$ for $k = 1, 2, 3$ and $\phi_{2,0,1}^1$.

B. Core-localized (advective) modes

A second, qualitatively distinct family is shown in Fig. 10. These eigenfunctions are sharply localized near the elliptic cores of regular islands and form compact, approximately circular patterns centered on the fixed point. Their structure and spectral organization are those of a two-dimensional harmonic oscillator: the modes appear in short ladders, typically in complex-conjugate pairs, with successive members exhibiting additional radial rings.

In this sense, these eigenfunctions are local Koopman modes of the integrable dynamics in the island core¹³. They represent a coherent rotation about the elliptic point, weakly damped by diffusion.

Like the island-filling modes, these eigenfunctions inherit a discrete phase label $m \in \{0, \dots, p-1\}$ associated with the p -fold island geometry. In addition, two internal indices are required to distinguish their oscillator structure: an azimuthal index q , which fixes the spectral phase of the eigenvalue, and a radial index k . We therefore denote this family by

$$\phi_{q,m,k}^p. \quad (13)$$

The physical meaning of the additional index q is rooted in the local Hamiltonian structure of an elliptic island core. In a neighborhood of an elliptic fixed point, the standard map is smoothly conjugate to a rotation in action-angle coordinates,

$$(I, \vartheta) \mapsto (I, \vartheta + \Omega(I)),$$

with $\Omega(I)$ approximately constant near the origin. In the absence of diffusion, scalar density in this region is simply transported by rigid rotation. The corresponding Koopman operator therefore admits Fourier modes $e^{iq\vartheta}$ as exact eigenfunctions, with eigenvalues $e^{iq\Omega}$.

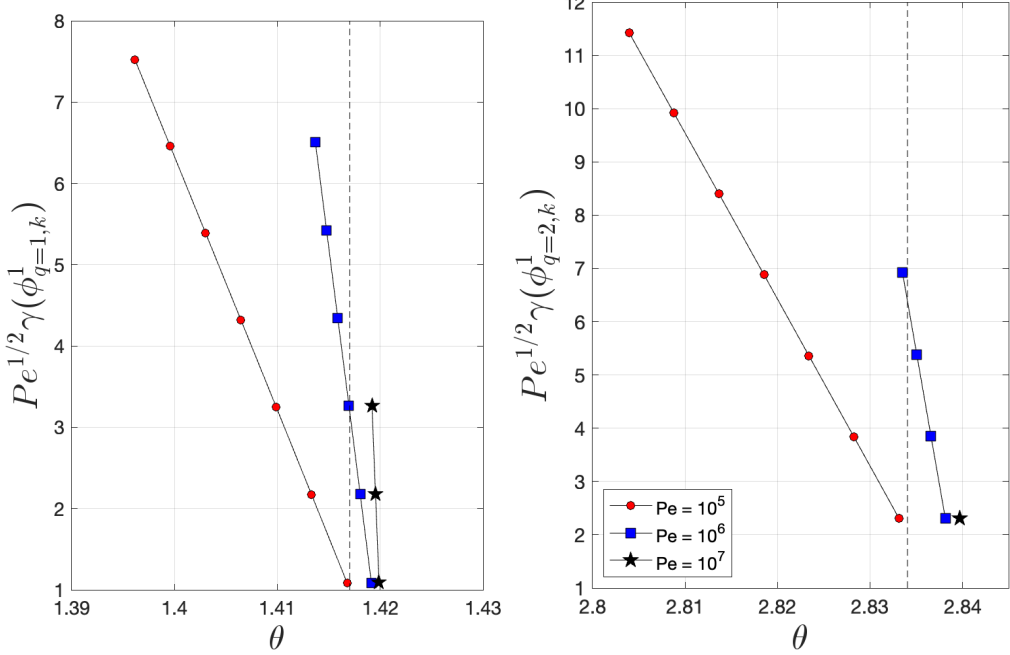


FIG. 11. Rescaled decay rate $\text{Pe}^{1/2} \gamma$ versus spectral phase θ for the dominant advective ladders in the period-1 island. Left: $q = 1$ branch. Right: $q = 2$ branch. The dashed line shows the geometric prediction $q\theta_{\text{adv}}$ obtained from the local island rotation frequency.

Finite diffusivity introduces weak transverse leakage across level sets of I , converting these neutral Koopman modes into slowly decaying eigenfunctions of the advection-diffusion operator. The integer q thus labels the azimuthal sector of the local rotation, while k counts radial excitations within the resulting harmonic well. The spectral phase

$$\theta = \arg(\lambda)$$

is therefore not arbitrary: it encodes the underlying Hamiltonian rotation frequency of the island core. In the raw spectra, this structure appears as discrete vertical bands in θ , one for each admissible value of q .

For weakly damped coherent rotation, diffusion acts only through slow transverse leakage, imposing linear scaling in the oscillator quantum number,

$$\gamma_k(\phi^p) \sim \sqrt{D} k. \quad (14)$$

The prefactor carries a weak dependence on the azimuthal index q through the local curvature of the island core: modes with larger q experience stronger azimuthal shear and therefore enhanced leakage, giving the refined estimate

$$\gamma_k \sim \sqrt{D} \sqrt{q} k.$$

This geometric q -dependence will determine where advective ladders first intersect the diffusive spectrum in Sec. VII.

Figure 11 isolates the dominant advective branches from the raw spectrum, rescales the decay rate by $\text{Pe}^{1/2}$, and displays the result in a narrow window of spectral phase θ for the primary azimuthal sectors $q = 1$ (left) and $q = 2$ (right). In these coordinates each family collapses onto a single slanted ladder, with successive k forming the expected harmonic-oscillator hierarchy.

Across three decades in Péclet number the points align rigidly and the spacing in k is preserved, confirming the $\text{Pe}^{-1/2}$ scaling predicted for advective (core-localized) modes^{19,20}.

The dashed line in each panel marks the geometric phase $q\theta_{\text{adv}}$ obtained directly from the local island rotation frequency; the observed branches follow this prediction without any spectral fitting. The small drift of θ toward smaller values with increasing k reflects azimuthal shear in the island core: higher k modes extend farther in radius and therefore experience slightly different rotation rates. Because diffusion spreads the modes across streamlines, the shear-induced phase shift decreases with increasing Pe as this cross-stream spreading weakens.

VII. GEOMETRIC PREDICTION OF SPECTRAL ORDERING

The classification developed above does more than organize the observed spectrum: it provides a concrete framework for predicting where distinct families of modes must appear in the ordered eigenvalue list. The slow spectrum is assembled from a finite collection of square-well ladders $\psi_{k,m}^p$, one for each regular island chain, together with harmonic-oscillator ladders $\phi_{q,m,k}^p$ associated with elliptic cores. Each ladder obeys a simple asymptotic law,

$$\gamma_k^{(p)} \sim D\alpha_p k^2, \quad \gamma_k^{(\phi)} \sim \sqrt{D}\beta_p k,$$

with prefactors α_p and β_p determined by geometric properties of the corresponding island: effective width for the square-well modes and local curvature of the Hamiltonian near the elliptic point for the oscillator modes.

A. Geometric predictors for inter-island hybridization

Within each regular island the diffusive spectrum organizes into a ladder of modes. The predictor developed here is based entirely on geometry and scaling, not on the spectrum itself. In a period- p island of area A_p , the k th diffusive mode is supported on structures of characteristic size

$$\ell_p(k) \sim \frac{\sqrt{A_p}}{k}.$$

Diffusion supplies a competing length scale, $\ell_D \sim \sqrt{D}$, which sets the smallest separation the operator can resolve.

Two ladders become eligible for hybridization when their associated geometric scales become comparable within diffusive resolution. For a fixed branch (p, k_p) and the period-1 ladder, we therefore monitor the scale mismatch

$$\delta_p(k) = |\ell_1(k) - \ell_p(k_p)| = \left| \frac{\sqrt{A_1}}{k} - \frac{\sqrt{A_p}}{k_p} \right|.$$

which is determined purely by island geometry and asymptotic scaling. Local minima of $\delta_p(k)$ identify those k for which the two ladders achieve their closest geometric commensurability. These minima are sharp and isolated, and their ordering is fixed in advance by geometry, independent of D .

Diffusion controls whether a given geometric commensurability is actually realized as a mixed eigenmode. The operator cannot resolve scale separations smaller than $\ell_D \sim \sqrt{D}$, so significant hybridization requires

$$\delta_p(k) \lesssim \mathcal{O}(\sqrt{D}).$$

At moderate D several shallow minima satisfy this criterion, leading to early and sometimes strong mixing between ladders. As D decreases, the resolvable threshold tightens: many

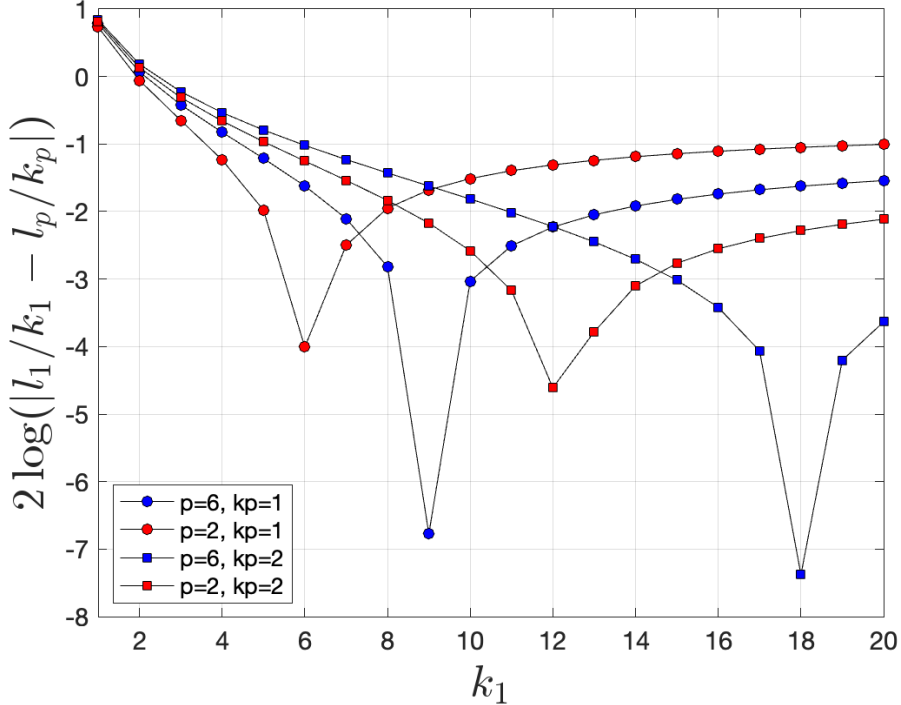


FIG. 12. Detuning diagnostic used to predict candidate inter-island interactions. For each k in the period-1 ladder we plot $2 \log_{10} \left| \lambda_k^{(1)}/k - \lambda_{k_p}^{(p)}/k_p \right|$ for $p \in \{2, 6\}$ and selected k_p .

candidate crossings devolve into weak, percent-level leakage between branches, while only the deepest geometric minima survive as genuine mixed modes.

Figure 12 shows $\delta_p(k)$ for the period-2 and period-6 branches against the period-1 ladder. Each curve consists of a sequence of sharp, isolated minima. These minima mark the discrete values of k for which the geometric length scale $\ell_1(k)$ most closely matches $\ell_p(k_p)$ for a given island. Their locations are fixed entirely by island areas and ladder indices; they therefore provide a purely geometric ordering of candidate inter-island interactions.

Diffusion does not determine where these minima occur. It determines which of them are dynamically relevant. At moderate D , several of the shallow minima lie within diffusive resolution and produce visibly mixed modes. As D decreases, the resolvable threshold tightens: most of these candidates devolve into weak, percent-level leakage, and only the deepest minima survive as genuine hybrid modes. In the $D \rightarrow 0$ limit, the first *strong* mixed mode converges toward the deepest geometric minimum, where the scale matching is most precise.

B. Geometric predictors for the onset of advective modes

A similar estimate governs the relative placement of diffusive and advective families. For a fixed advective family (phase index) q , the first core-localized mode $\phi_{q,1}^1$ satisfies

$$\gamma_{q,1}^{(\phi)} \sim \sqrt{D} \beta_q.$$

Equating this with the k th diffusive mode of the period-1 island gives

$$D \alpha_1 k^2 \approx \sqrt{D} \beta_q, \quad k^*(q) \sim D^{-1/4} (\beta_q / \alpha_1)^{1/2}.$$

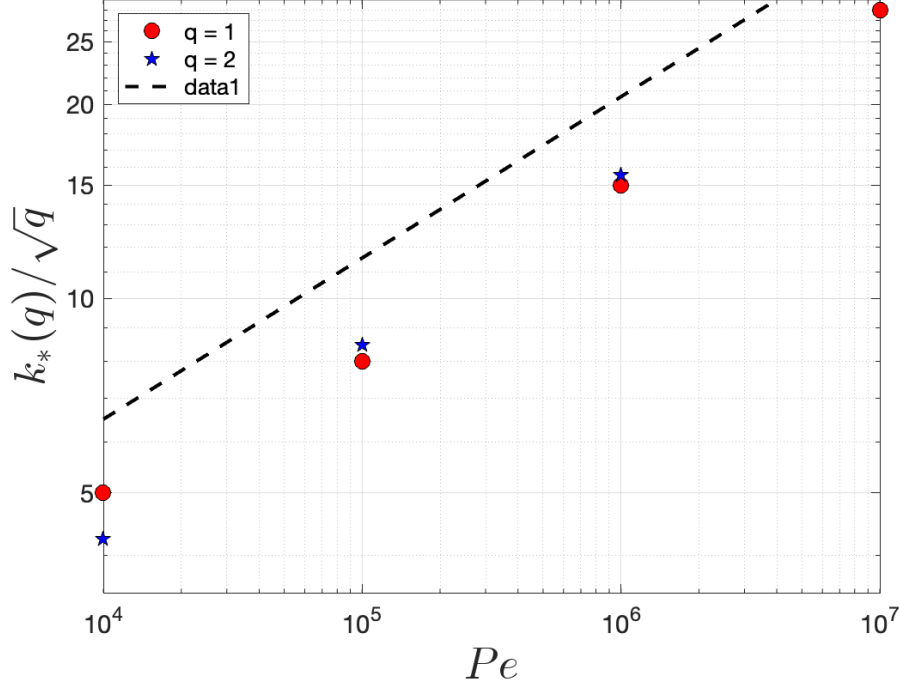


FIG. 13. Normalized crossover index $k^*(q)/\sqrt{q}$ versus Pe for two advective families on the period-1 island ($q = 1$ circles, $q = 2$ markers). The dashed line indicates the predicted scaling $k^* \propto Pe^{1/4}$, demonstrating collapse across q .

Thus the number of diffusive modes lying below a given advective ladder grows as $D^{-1/4}$ (equivalently $k^* \propto Pe^{1/4}$), explaining quantitatively why the Koopman ladders retreat to higher and higher indices as Pe increases. Different advective families share the same exponent but may differ in prefactor through the family-dependent constants β_q .

Figure 13 verifies this prediction directly. For each family we define $k^*(q)$ as the largest diffusive index whose decay rate remains below that of the leading core-localized mode. The measured crossover indices collapse onto straight lines in log-log coordinates with slope 1/4, in agreement with the $D^{-1/4}$ scaling. The two families are approximately parallel but offset, indicating that the exponent is universal while the prefactor depends on the local structure of the corresponding elliptic region.

The estimates depend on local geometric information: island area, effective width, and curvature near elliptic points. No global spectral computation is required to determine the scaling of the crossover. From phase-space geometry alone, one may estimate which island families contribute the slowest diffusive modes, where advective families first enter the ordered spectrum, and when tunneling between branches occurs.

The mixed Hamiltonian geometry directly determines the organization of the advection-diffusion spectrum: which island families contribute the slowest modes, where advective families enter, and when hybridization occurs. The precise placement of individual modes remains sensitive to finite- Pe corrections and hybridization.

VIII. CONCLUSIONS

We have examined the spectral properties of the one-period advection-diffusion operator in a prototypical area-preserving map with mixed phase space. By combining direct numerical computations at Péclet numbers as large as 10^7 with a semiclassical interpretation based on the effective parameter $\hbar_{\text{eff}} = \sqrt{D}$, we have shown that a substantial portion of

the slow spectrum admits a rigid geometric organization.

IX. CONCLUSIONS

We have examined the spectral properties of the one-period advection-diffusion operator in a prototypical area-preserving map with mixed phase space. By combining direct numerical computations at Péclet numbers as large as 10^7 with a semiclassical interpretation based on the effective parameter $\hbar_{\text{eff}} = \sqrt{D}$, we have shown that a substantial portion of the slow spectrum admits a rigid geometric organization. Individual eigenmodes may be associated with specific phase-space structures: modes supported on entire islands behave as square-well states, modes localized near elliptic fixed points form harmonic-oscillator ladders, and additional diffusive modes arise from weak coupling between dynamically separated islands.

The semiclassical viewpoint provides not only a qualitative framework for interpreting these observations but also quantitative predictions for spectral scaling and multiplicity. In particular, the number of diffusive modes supported on a given island and their decay-rate scaling follow directly from the size of the corresponding invariant set and the dependence of \hbar_{eff} on D . The close agreement between these predictions and the numerical results confirms that the observed organization is controlled by the underlying Lagrangian geometry rather than by accidental features of discretization or parameter choice. While individual scaling laws have been established for limiting cases— $\text{Pe}^{-1/2}$ for integrable flows^{19,20} and Pe^{-1} for dominant island modes^{17,18}—the present work demonstrates how these families coexist and compete across the full slow spectrum.

Inter-island coupling plays a central role in shaping the slow spectrum. At finite diffusivity we observe mixed eigenfunctions whose supports span multiple dynamically separated islands. Our geometric resonance model shows that this hybridization is not a monotone finite-diffusivity effect that simply disappears as $D \rightarrow 0$; instead, it is selected by near-commensurabilities between island areas and local length scales, and therefore can recur at moderate values of the radial index k even at very small D . This provides a geometric explanation for the near-degeneracies observed by Popovych et al.¹¹, which were found to vary unpredictably in parameter space. Mixed diffusive structures thus persist in the slow spectrum in a geometry-controlled way.

As Péclet number increases, the advective (Koopman) modes retreat to higher and higher indices, consistent with the $\text{Pe}^{1/4}$ scaling derived in Sec. VII A. As a result, for any fixed mode count N , the first N eigenmodes become increasingly dominated by diffusive, square-well-like island families. In this sense, finite-mode spectral approximations become effectively self-adjoint as $\text{Pe} \rightarrow \infty$: the leading modes are increasingly well described by self-adjoint diffusive operators on individual regular sets.

This reorganization by mode number, however, does not imply that advective modes become dynamically irrelevant. For modes slower than a fixed decay rate γ^* —the physically meaningful criterion for finite-time dynamics—both diffusive and advective families contribute $O(\sqrt{\text{Pe}})$ modes, with their ratio determined by geometric prefactors independent of Pe . The $\text{Pe}^{1/4}$ crossover reorganizes where families appear in the ordered spectrum but does not change their relative importance for finite-time dynamics. The practical consequence is that spectral approximations based on fixed mode counts (common in reduced-order models) capture increasingly diffusive character, while approximations based on fixed timescales retain balanced contributions from both families.

An important consequence of this structure is the absence of any a priori geometric control over spectral gaps within the slow manifold. While the underlying phase-space geometry predicts where competing diffusive ladders approach one another, the resulting interactions generically produce avoided crossings whose detailed splittings depend on fine-scale structure. As a result, the ordering and separation of decay rates within the slow spectrum are not monotone functions of island size or resonance order. Mixed modes therefore disrupt any simple hierarchy of time scales, and preclude a universal geometric ranking of finite-time decay channels.

These results show that the slow decay of passive scalars in mixed phase spaces is governed neither by a uniform chaotic mechanism nor by a single dominant eigenmode, but by a semiclassical partitioning of phase space. Invariant sets of the Lagrangian dynamics imprint themselves directly on the spectrum, giving rise to multiple long-lived decay channels whose scaling, multiplicity, and ordering are fixed by geometry but modulated by resonance. Mixed phase spaces therefore admit a natural spectral language for transport, in which Lagrangian structure determines not only where scalars persist, but how the entire slow spectrum is organized.

The analysis presented here suggests several directions for future work, including extensions to continuously driven or aperiodic flows, the role of island breakup and transport barriers in higher dimensions, and the impact of stochastic perturbations on semiclassical scaling. More broadly, the emergence of geometry-controlled spectral families highlights mixed Hamiltonian systems as a natural setting in which quantum-inspired ideas can be fruitfully applied to classical transport problems.

- ¹H. Aref *et al.*, “Frontiers of chaotic advection,” *Reviews of Modern Physics* **89**, 025007 (2017).
- ²A. Babiano, G. Boffetta, A. Provenzale, and A. Vulpiani, “Chaotic advection in point vortex models and two-dimensional turbulence,” *Physics of Fluids* **6**, 2465–2474 (1994).
- ³T. Benzekri, C. Chandre, X. Leoncini, R. Lima, and M. Vittot, “Chaotic advection and targeted mixing,” *Physical Review Letters* **96** (2006).
- ⁴C. Schlick, R. M. Lueptow, and K. D. Dorfman, “Interplay between chaos and diffusion in time-periodic sine flow,” *Physics of Fluids* **25**, 103602 (2013).
- ⁵C. Lopez, Z. Neufeld, E. Hernandez-Garcia, and P. H. Haynes, “Chaotic advection of reacting substances: Plankton dynamics on a meandering jet,” *Physics and Chemistry of the Earth Part B: Hydrology, Oceans and Atmosphere* **26**, 313–317 (2001).
- ⁶S. Prants, M. Budyansky, V. Ponomarev, and M. Uleysky, “Lagrangian study of transport and mixing in a mesoscale eddy street,” *Ocean Modelling* **38**, 114–125 (2011).
- ⁷T. M. Elgindi, K. Liss, and J. C. Mattingly, “Optimal enhanced dissipation and mixing for a time-periodic, lipschitz velocity field on \mathbb{T}^2 ,” *Duke Mathematical Journal* **174**, 1209–1260 (2025).
- ⁸R. T. Pierrehumbert, “Tracer microstructure in the large-eddy dominated regime,” *Chaos Solitons & Fractals* **4**, 1091–1110 (1994).
- ⁹V. Toussaint, P. Carrière, J. Scott, and J.-N. Gence, “Spectral decay of a passive scalar in chaotic mixing,” *Physics of Fluids* (1994–present) **12**, 2834–2844 (2000).
- ¹⁰B. Sundaram, A. C. Poje, and A. K. Pattanayak, “Persistent patterns and multifractality in fluid mixing,” *Phys. Rev. E* **79**, 066202 (2009).
- ¹¹O. V. Popovych, A. Pikovsky, and B. Eckhardt, “Abnormal mixing of passive scalars in chaotic flows,” *Physical Review E* **75**, 036308 (2007).
- ¹²I. Mezić, “Spectral properties of dynamical systems, model reduction and decompositions,” *Nonlinear Dynamics* **41**, 309–325 (2005).
- ¹³I. Mezić, “Analysis of fluid flows via spectral properties of the koopman operator,” *Annual Review of Fluid Mechanics* **45**, 357–378 (2013).
- ¹⁴G. Froyland, “Transport in dynamical systems: coherent sets,” *Communications in Mathematical Physics* **268**, 413–449 (2010).
- ¹⁵M. Giona, S. Cerbelli, and A. Adrover, “Spectral properties and transport mechanisms of partially chaotic bounded flows in the presence of diffusion,” *Physics of Fluids* **16**, 141–154 (2004).
- ¹⁶S. Cerbelli, V. Vitacolonna, A. Adrover, and M. Giona, “Eigenvalue-eigenfunction analysis of infinitely fast reactions and micromixing regimes in regular and chaotic bounded flows,” *Chem. Eng. Sci.* **59**, 2125–2144 (2004).
- ¹⁷O. Gorodetskyi, M. F. M. Speetjens, and P. D. Anderson, “An efficient approach for eigenmode analysis of transient distributive mixing by the mapping method,” *Physics of Fluids* **24**, 053602 (2012).
- ¹⁸O. Gorodetskyi, M. Giona, and P. D. Anderson, “Spectral analysis of mixing in chaotic flows via the mapping matrix formalism: Inclusion of molecular diffusion and quantitative eigenvalue estimate in the purely convective limit,” *Physics of Fluids* **24**, 073603 (2012).
- ¹⁹J. Vukadinovic, E. Dredits, A. C. Poje, and T. Schäfer, “Averaging and spectral properties for the 2d advection–diffusion equation in the semiclassical limit,” *Physica D* **310**, 1–18 (2015).
- ²⁰J. Bedrossian and M. Coti Zelati, “Enhanced dissipation, hypoellipticity, and anomalous small noise inviscid limits in shear flows,” *Archive for Rational Mechanics and Analysis* **224**, 1161–1204 (2017).
- ²¹J. Vukadinovic, “The limit of vanishing diffusivity for passive scalars in hamiltonian flows,” *Archive for Rational Mechanics and Analysis* **242**, 1395–1444 (2021).
- ²²B. V. Chirikov, “A universal instability of many-dimensional oscillator systems,” *Physics Reports* **52**, 263–379 (1979).
- ²³R. B. Lehoucq, D. C. Sorensen, and C. Yang, *ARPACK Users’ Guide: Solution of Large-Scale Eigenvalue Problems with Implicitly Restarted Arnoldi Methods* (Society for Industrial and Applied Mathematics, Philadelphia, PA, 1998).

APPENDIX A: NUMERICAL IMPLEMENTATION

The leading eigenvalues and eigenfunctions of the advection-diffusion operator are computed using an implicitly restarted Arnoldi method as implemented in ARPACK²³. The operator is never formed explicitly. Instead, ARPACK is supplied with a matrix-vector product routine that applies one step of the Fourier-space transfer operator to an input vector. All iterations therefore operate in a matrix-free setting, with the computational cost dominated by repeated evaluations of this operator.

The state is represented in Fourier space on a square spectral grid

$$(m, n) \in \{-l, \dots, l\}^2,$$

so that the dimension of the eigenproblem is

$$N = (2l + 1)^2.$$

The integer l is read from an external parameter file and directly controls the spatial resolution. When eigenfunctions are reconstructed in physical space, they are interpreted on an $N_x \times N_x$ grid with $N_x = 2l + 1$ points in each direction, corresponding to a periodic domain of size $2\pi \times 2\pi$ and grid spacing $\Delta x = \Delta y = 2\pi/(2l + 1)$.

The matrix-vector product implements the one-step advection-diffusion operator in Fourier space,

$$\rho_{m,n}^{t+1} = e^{-D(m^2+n^2)} \sum_k J_{m-k}(n\kappa) \rho_{k,k+n}^t,$$

with truncation-aware bounds on the summation index k to ensure that all accessed modes remain within the spectral domain. Here J_q denotes the Bessel function of the first kind, κ is the map amplitude, and D is the diffusion coefficient. The Bessel weights $J_q(n\kappa)$ are precomputed once at startup. The operator is applied by direct convolution and index shifting in coefficient space, and is parallelized with OpenMP over Fourier modes.

The Arnoldi iteration targets the eigenvalues of largest magnitude, corresponding to the least damped modes of the transfer operator. Convergence is assessed using the standard relative residual

$$\frac{\|Av - \lambda v\|_2}{|\lambda|}.$$

Typical runs achieve residuals of order 10^{-14} , consistent with double-precision accuracy. The total cost of a computation is well characterized by the number of operator applications reported by ARPACK, with each application corresponding to one evaluation of the Fourier-space advection-diffusion operator.

As a representative high-resolution case, we consider $\kappa = 1.7$ and $l = 600$, for which the eigenproblem has dimension

$$N = (2l + 1)^2 = 1201^2 \approx 1.44 \times 10^6,$$

and the reconstructed eigenfunctions are resolved on a 1201×1201 physical grid with spacing $\Delta x = 2\pi/1201 \approx 7.8 \times 10^{-3}$. For this problem, even at very weak diffusion ($D = 10^{-7}$), the Arnoldi iteration converges to all requested eigenpairs with relative residuals

$$\frac{\|Av - \lambda v\|_2}{|\lambda|} \lesssim 10^{-12},$$

with the majority of modes achieving residuals at the 10^{-13} – 10^{-14} level. These values are far below any physically meaningful scale associated with the discretized operator and indicate that the computed eigenpairs are accurate to essentially machine precision. The computational effort in this regime corresponds to $\mathcal{O}(10^3)$ applications of the Fourier-space operator.

Spatial Resolution and Spectral Adequacy

The choice of truncation $l = 600$ is governed by the exponential damping inherent to the diffusive operator. The factor $e^{-D(m^2+n^2)}$ in the Fourier-space evolution operator suppresses contributions from high wavenumbers at a rate that depends directly on the diffusivity. At the weakest diffusion considered here ($D = 10^{-7}$), Fourier modes with $|m|$ or $|n|$ exceeding

$$k_c \approx \sqrt{\frac{-\ln \epsilon}{D}} \approx \sqrt{\frac{32}{D}} \approx 566$$

contribute less than $\epsilon = 10^{-14}$ to the operator in spectral norm, and are therefore below the numerical precision of the computation. The truncation at $l = 600$ thus captures all dynamically significant modes, with a safety margin of approximately six percent.

Spectral convergence is further supported by three independent consistency checks. First, the tight Arnoldi residuals reported above confirm that the computed eigenpairs are converged to machine precision within the chosen Fourier basis. Second, the collapse of rescaled eigenvalue families onto universal curves across three decades in Péclet number (Figs. 9, 11, 13) demonstrates that the computation has reached the asymptotic weak-diffusion regime in which the predicted scaling laws hold. Systematic under-resolution would manifest as a drift or scatter in these scalings; none is observed. Third, the ordering and multiplicity of spectral families matches the predictions derived from phase-space geometry in Section VII, providing an independent geometric validation of the numerical results. Additionally, Fourier truncation strategies at comparable or coarser resolution have been validated for related advection-diffusion problems with mixed phase spaces^{15,17,18}, where spectral convergence and modal structure were shown to be robust to discretization parameters in the weak-diffusion limit.

These diagnostics, taken together with the exponential filtering built into the operator itself, provide strong evidence that the reported spectra are fully resolved and that the observed organization into diffusive, advective, and tunneling families is a robust feature of the continuum problem rather than an artifact of discretization.

APPENDIX B: LOCAL HAMILTONIAN GEOMETRY OF REGULAR ISLANDS

The interpretation of the slow spectrum in terms of square-well and oscillator families relies on geometric properties of the regular islands of the underlying Lagrangian map. For each elliptic island we construct a local effective Hamiltonian $H_{\text{eff}}(x, y)$ whose level sets coincide with invariant curves of the map. This provides two geometric parameters that govern the slow spectrum: an island scale α , proportional to the square root of the island area, which controls the spacing of diffusive modes, and a core curvature β , the quadratic coefficient of H_{eff} at the elliptic fixed point, which controls the spacing of advective modes. We document how these quantities are obtained directly from the map, without reference to any spectral computation.

Reconstructing H_{eff}

Let (x_*, y_*) be an elliptic fixed point of the map. We initialize trajectories at small offsets $(x_* + r, y_*)$ and iterate the map for $N \gg 1$ steps, discarding an initial transient. The angular advance per iterate yields a local rotation number $\rho(r)$. Integrating this profile defines an effective action variable

$$I(r) = \int_0^r \rho(s) ds, \quad (15)$$

and hence an effective Hamiltonian $H_{\text{eff}}(I)$ satisfying $\Omega(I) = dH_{\text{eff}}/dI = \rho$. Mapping this relation back into physical space produces $H_{\text{eff}}(x, y)$ whose contours coincide with invariant

curves of the island. Figure 1 shows reconstructed H_{eff} for the period-1 and period-6 islands at $K = 1.7$.

Island scale and diffusive modes

The outer boundary of each island forms a finite barrier for diffusion. The effective well width α_p is defined by

$$\alpha_p^2 \equiv \frac{1}{\pi} \text{Area(island } p\text{)}, \quad (16)$$

so that α_p is the radius of a disk with the same area. Diffusion inside an island is approximately isotropic, so the slowest modes supported on the island behave as Laplacian eigenfunctions on a bounded domain of size α_p , yielding the scaling

$$\gamma_k(\psi^p) \sim D \alpha_p^{-2} k^2. \quad (17)$$

Differences in α_p determine where modes from different island families appear in the global spectrum.

Core curvature and advective modes

Near the elliptic fixed point, H_{eff} admits a quadratic expansion

$$H_{\text{eff}}(I) = H_0 + \frac{1}{2} \beta_p I^2 + O(I^3), \quad (18)$$

with $\beta_p = d\Omega/dI|_{I=0}$. This curvature fixes the local oscillator frequency and hence the spacing of the advective ladder $\phi_{q,k,m}^p$. Diffusion introduces a transverse length scale $O(\sqrt{D})$ in action space, so that the oscillator spectrum obeys

$$\gamma_k(\phi^p) \sim \sqrt{D} \beta_p^{1/2} k. \quad (19)$$

Spectral phase and advective branches

For an eigenvalue $\lambda = |\lambda| e^{\pm i\theta}$ of the one-period advection-diffusion operator, the argument θ encodes the rotation frequency of the underlying Koopman mode. Near an elliptic fixed point, the effective Hamiltonian provides a local rotation frequency $\Omega_0 \approx \Omega(I)|_{I=0}$, which defines a fundamental advective phase

$$\theta_{\text{adv}} = \Omega_0. \quad (20)$$

Advective modes are organized by azimuthal wavenumber q , corresponding to the number of windings around the elliptic core. Modes with azimuthal index q rotate q times per iterate, producing spectral phases

$$\theta_q = q \theta_{\text{adv}} \pmod{2\pi}. \quad (21)$$

In the raw spectra (Fig. 4), this appears as families of eigenvalues aligned along discrete rays at $\theta = q \theta_{\text{adv}}$, forming the vertical alignment bands visible in the spectral plots. The radial index k within each azimuthal family labels successive radial excitations at fixed q , corresponding to progressively larger action levels I_k and additional radial nodes in the eigenfunction.

As D decreases, more radial levels become resolved within each azimuthal sector, and the discrete harmonic structure $\{q \theta_{\text{adv}}\}$ becomes increasingly apparent. In the limit $D \rightarrow 0$, the spectrum approaches a continuous arc on the unit circle, consistent with the continuous Koopman spectrum of the diffusion-free map, but retains the discrete harmonic organization imposed by the elliptic core geometry.